Photoacoustics 32 (2023) 100535

Contents lists available at ScienceDirect

Photoacoustics

journal homepage: www.elsevier.com/locate/pacs

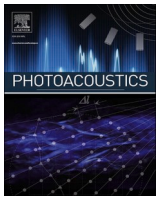

An extremum-guided interpolation for sparsely sampled photoacoustic imaging

Haoyu Wang [a], Luo Yan [b], Cheng Ma [b,1], Yiping Han [c,*]

[a] Hangzhou Institute of Technology, XIDIAN University, Hangzhou 311231, Zhejiang, China
[b] Department of Electronic Engineering, Tsinghua University, Beijing 100084, China
[c] School of Physics, XIDIAN University, Xi'an 710126, Shaanxi, China

ARTICLE INFO

OCIS:
170.5120
170.3010
110.3000
100.2960

Keywords:
Photoacoustic imaging
Signal processing
Interpolation algorithm
Image reconstruction
Image quality assessment

ABSTRACT

In photoacoustic (PA) reconstruction, spatial constraints or real-time system requirements often result to sparse PA sampling data. For sparse PA sensor data, the sparse spatial and dense temporal sampling often leads to poor signal continuity. To address the structural characteristics of sparse PA signals, a data interpolation algorithm based on extremum-guided interpolation is proposed. This algorithm is based on the continuity of the signal, and can complete the estimation of high sampling rate signals without complex mathematical calculations. PA signal data is interpolated and reconstructed, and the results are evaluated using image quality assessment methods. The simulation and experimental results show that the proposed method performs better than several typical algorithms, effectively restoring image details, suppressing the generation of artifacts and noise, and improving the quality of PA reconstruction under sparse sampling.

1. Introduction

Photoacoustic (PA) imaging is an emerging non-destructive testing technique based on the PA effect discovered by Bell [1]. By irradiating biological tissue with pulsed laser sources, the local temperature change caused by the absorption of short-pulsed laser irradiation can cause tissue elastic deformation, thereby generating sound waves [2]. Due to the differences in absorption characteristics of different tissues, the transformation of PA signals can reflect their distribution, so the internal structure of objects can be reconstructed based on the ultrasound signals generated by pulsed excitation. PA imaging has the advantages of high resolution of optical imaging and high imaging depth of ultrasound imaging, as well as good biological safety [3,4]. The complete process of PA reconstruction is shown in Fig. 1. According to the characteristics of the PA reconstruction process, it can be divided into three main parts, namely, data acquisition and processing, image reconstruction, and reconstructed image processing. Based on the different parts of the reconstruction process, the relevant algorithms can also be divided into three categories, namely, image reconstruction algorithms, image processing algorithms, and data signal processing algorithms.

In image reconstruction algorithms, traditional algorithms include direct back-projection (BP), and delay and sum (DAS), which estimate the original sound pressure distribution based on the spatial relationship between signal data and the reconstruction target [5]. However, these methods may generate artifacts in sparse sampling situations. The time-reversal (TR) reconstruction algorithm, proposed by Fink and Prada [6], is significantly different from traditional reconstruction algorithms. It is a reconstruction algorithm that estimates the original sound pressure distribution by backward propagation of the temporal signal data [7]. The introduced artifact noise is weak, and fewer constraints are required for reconstruction [8].

Image processing algorithms mainly deal with the reconstruction results that have been obtained. Traditional image processing methods such as filtering, contrast enhancement [9,10], etc, have been applied in PA imaging for a long time. In recent years, methods such as dictionary learning and deep learning [11,12] have also been applied to post-processing of PA images and achieved good results. However, as post-processing methods, they have inherent limitations and cannot accurately restore lost information in the reconstructed images.

As for data preprocessing methods, due to the similar characteristics

* Corresponding author.
E-mail address: hanyp@mail.xidian.edu.cn (Y. Han).
[1] Co-author

https://doi.org/10.1016/j.pacs.2023.100535
Received 31 May 2023; Received in revised form 13 July 2023; Accepted 17 July 2023
Available online 19 July 2023

of PA data and CT data, methods such as wavelet transform and signal deconvolution derived from CT signal processing have also achieved good results in PA signal processing [13–15]. In addition to necessary preprocessing operations such as signal denoising and alignment, signal data interpolation is an important means to improve the quality of PA reconstruction. Traditional interpolation methods include nearest neighbor interpolation (NI), linear interpolation(LI), spline interpolation(SI) [16–18], etc. These traditional methods treat signal vectors or matrices as sparse grids and estimate the possible signal values at the interpolation positions in the sparse grid by analyzing the relationship between the current element and its neighboring elements and fitting them with linear relationships. However, the relative relationship between signals is not always limited to the neighborhood, which mainly depends on the characteristics and sampling methods of different signals. Different from traditional algorithms, the New edge-directed interpolation (NEDI) [19,20] algorithm utilize the geometric duality between the covariance of low-resolution and high-resolution images to compute the values of pixels needed to be inserted in the high-resolution image, which can effectively discern the edge information of the image and achieve high-quality interpolation for signals with continuous edge features. Compressed sensing (CS) [21,22], which is also a typical nonlinear signal processing algorithm, it exploits the sparsity of signals to acquire their discrete samples through random sampling at a much lower rate than the Nyquist sampling rate, and then perfectly reconstructs the signals through nonlinear reconstruction algorithms. Other methods such as support vector machines and deep learning [23,24] have also achieved good results in PA data processing, but they mainly use a large amount of data and parameters to fit the optimal solution, which is quite different from the method of estimating high sampling rate signals through analysis and calculation.

Researchers have conducted in-depth studies on the causes of artifacts in the reconstruction process, and the results show that when the PA data is sufficiently dense, artifacts in the reconstruction can be significantly reduced [25]. Among the aforementioned reconstruction methods, BP, DAS, and TR, are closely related to the quality of the PA signal sampling, and interpolation methods therefore have an important impact on PA reconstruction. Among interpolation methods, machine learning-based interpolation methods have better performance, but they require a large amount of work and high computational performance requirements, making it difficult to meet real-time and fast application scenarios. Mainstream computational interpolation methods are faster and can effectively improve the quality of PA reconstructed images, but often perform poorly in sparse sampling scenarios. With the continuous development of ultrasound transducer technology and processes, the working frequency of PA signals continues to increase [26], which makes the sparsity problem of PA signals mainly due to their spatial sampling density. In practical applications, the sparsity of PA signals can be caused by limitations in application scenarios and sensor sizes, or by actively reducing sampling density to increase the efficiency of PA imaging systems.

To improve the accuracy of PA signal interpolation under sparse sampling, this paper proposes a novel extremum-guided interpolation (EGI) algorithm based on the structural characteristics of sparse signals. The algorithm utilizes the continuity of PA signals in the temporal and spatial domains and achieves interpolation of sparse signals using a simple extremum function. Compared to methods such as NEDI and CS, the proposed method does not require complex calculations, and it can effectively improve the quality of PA reconstruction under sparse sampling. Image quality assessment (IQA) is used in simulation to evaluate the reconstruction results and compare the performance of various algorithms under various conditions. The simulation and experiment results show that the proposed method has better performance in sparse reconstruction.

2. Extremum-guided interpolation

2.1. EGI algorithm

To enhance the quality of reconstructed images, spatial interpolation is required for the acquired PA signal data before image reconstruction. The EGI algorithm uses a combination of nonlinear functions within a certain search range to select local extremum signals as interpolation signals, thus approximating the high-sampling rate signal.

During the sound pressure signal acquisition with a full-ring sensor array, assuming there are m sensors and n total time-domain sampling points, generally $n \gg m$, the signal data format is a matrix of size $m \times n$. For an ring sensor array, the matrix can be expanded by adding an extra row, where the first m rows are the same as the signal data matrix, and the $(m+1)$-th row vector is the same as the first row vector of the signal data matrix, resulting in a matrix $\mathbf{A}$ of size $(m+1) \times n$.

Let x_i denote the i-th row vector of matrix $\mathbf{A}$, $x_i(k)$ denote the k-th element of the i-th row vector of matrix $\mathbf{A}$, y_j denote the interpolated vector between x_j and x_{j+1}, and $y_j(k)$ denote the k-th element of y_j. Here, $i = 1,2,.,(m+1), j = 1,2,.,m$, $k = 1,2,.,n$, and the search half-width is set as d.

Firstly, linear interpolation is performed on the part of the matrix within a distance of d from the edge, namely the elements satisfying the condition $k = 1,2,.,d,(n-d+1),(n-d+2),.,n$, as shown in Eq. (1):

$$y_j(k) = \frac{x_j(k) + x_{j+1}(k)}{2}, \tag{1}$$

Next, we process the elements satisfying $k = (d+1),(d+2),.,(n-d)$ in vectors x_j and x_{j+1}. Based on the continuity of signals in the spatial dimension, the signal combinations in symmetric position regions can be roughly classified into three categories: "signal and signal," "signal and background," and "background and background." To determine the possible signals at the interpolation position, a minimum value function can be used for a simple judgment process, as shown in Fig. 2.

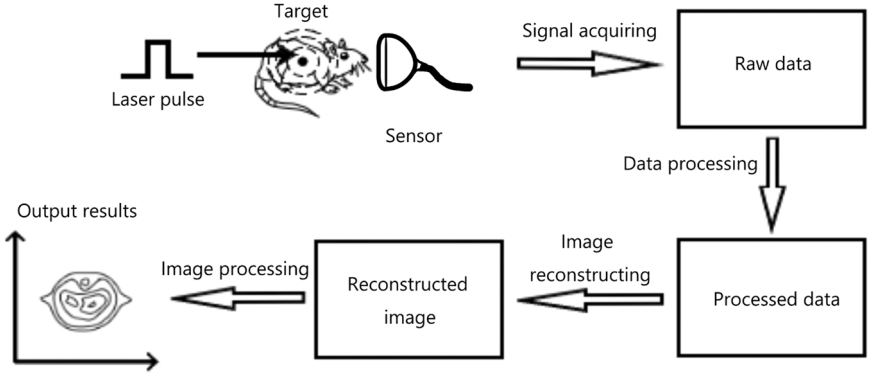

Fig. 1. PA imaging.

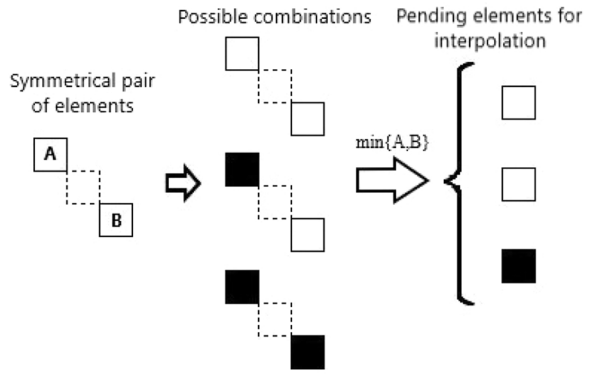

Fig. 2. Data interpolation process (White represents background, black represents signal).

Since the use of functions is mainly for judging the amplitude of the signal, the simultaneous occurrence of positive and negative signals may cause the function output to be abnormal. Therefore, the selection is decomposed into two parts deviating from the reference value:

$$\begin{aligned} \alpha_j(k) &= \{ \quad x_j(k), x_j(k) > 0 \quad 0, x_j(k) \le 0, \\ \beta_j(k) &= \{ \quad x_j(k), x_j(k) < 0 \quad 0, x_j(k) \ge 0, \end{aligned} \tag{2}$$

Among them, $\alpha_j(k)$ represents the k-th pixel of the positive vector α_j, and $\beta_j(k)$ represents the k-th pixel of the negative vector β_j.

Following the logic in Fig. 2, the signal is processed by comparing the elements corresponding to the symmetric center in two rows of vectors, and the minimum value is taken:

$$\begin{aligned} p_l(k) &= \min\{\alpha_j(k-d+l), \alpha_{j+1}(k+d-l)\}, \\ n_l(k) &= \min\{-\beta_j(k-d+l), -\beta_{j+1}(k+d-l)\}, \end{aligned} \tag{3}$$

Using the minimum value function within a certain search width centered at the k-th pixel, sets of values $\{p_1(k), p_2(k), ., p_d(k)\}$ and $\{n_1(k), n_2(k), ., n_d(k)\}$ can be obtained with the k-th pixel as the symmetric center. Those sets of values not only includes possible signal values but also possible background signal values. In order to screen out the background signal values contained therein and to select the most likely signal values at the corresponding position, a simple maximum value function can be used to process the results obtained from Eq. (3) based on the continuity of signals in the time dimension, as shown in Fig. 3.

Following the above method, the elements $p_l(k)$ and $n_l(k)$ satisfying the conditions $l = 1, 2, ., d$ are separately processed using the maximum value function:

$$\begin{aligned} P_l(k) &= \max\{p_1(k), p_2(k), ., p_d(k)\}, \\ N_l(k) &= \max\{n_1(k), n_2(k), ., n_d(k)\}, \end{aligned} \tag{4}$$

By adding the sign according to the positive or negative nature of the signal, the expression of the interpolation result $y_j(k)$ can be obtained as:

$$y_j(k) = P_l(k) - N_l(k) \tag{5}$$

Vector y_j is composed of $y_j(k)$ and inserted between vectors x_j and x_{j+1} in matrix **A**. The above process is repeated from $j = 1$ to $j = m$ in order, and the $(2m) \times n$ interpolation result matrix **B** is obtained by removing the $(2m + 1)$-th row vector as follows:

$$\mathbf{B} = \begin{bmatrix} x_1(1) & x_1(2) & \cdots & x_1(n) \\ y_1(1) & y_1(2) & \cdots & y_1(n) \\ x_2(1) & x_2(2) & \cdots & x_2(n) \\ \vdots & \vdots & \ddots & \vdots \\ x_m(1) & x_m(2) & \cdots & x_m(n) \\ y_m(1) & y_m(2) & \cdots & y_m(n) \end{bmatrix}, \tag{6}$$

Since the iterative interpolation method is based on row vectors, the interpolation rate of this method should be 2^N, where N is the number of iterations. The processing process is shown in Fig. 4.

2.2. Input parameters

From the principles of the EGI algorithm described earlier, it can be inferred that the only tunable parameter for the EGI algorithm is the search half-width d. For photoacoustic imaging using a ring array sensor, the selection of this parameter can be determined by the structural parameters of the array itself.

Due to differences in the distribution of sensors, the time at which the same signal is received by different sensors will vary slightly. Generally, when the sound pressure signal is in the internal region of the array, the closer the signal source is to the edge of the sensor array, the longer the time interval between adjacent sensors receiving the signal. The geometric relationship is shown in Fig. 5.

There, *Sensor*1 represents the sensor used as a reference for the current search half-width, *Sensor*2 represents the adjacent sensor on the same side as the signal source, and *Sensor*2* represents the adjacent sensor on the opposite side of the signal source. Therefore, L_1 denotes the distance between the source and *Sensor*2*, L_2 denotes the distance between the source and *Sensor*1, and L_3 denotes the distance between the source and *Sensor*2. R is the radius of the sensor array, r represents the radius of the arc formed by the possible locations of the signal

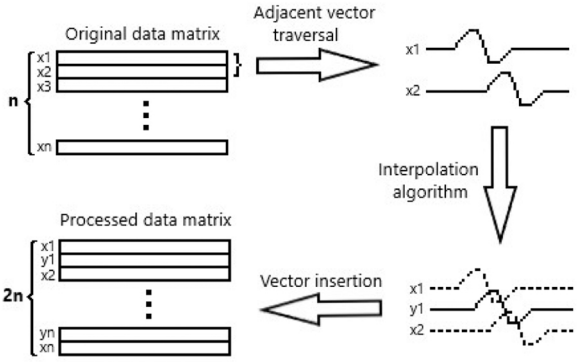

Fig. 4. Data interpolation process.

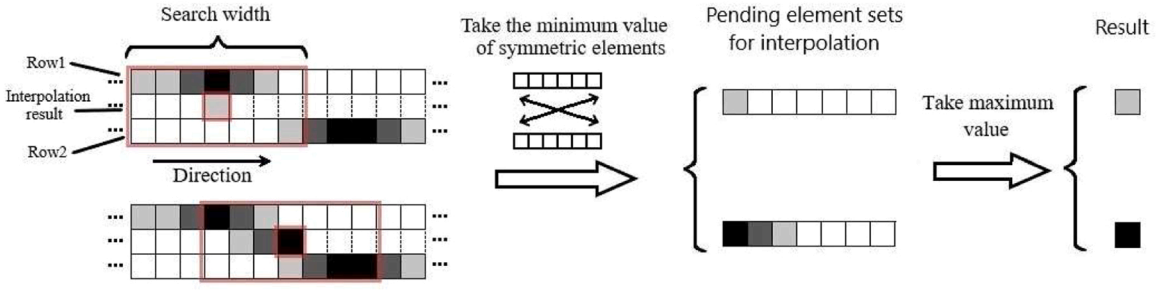

Fig. 3. Filter signal with extremal function (The gray depth represents the strength of the signal, with white being the background).

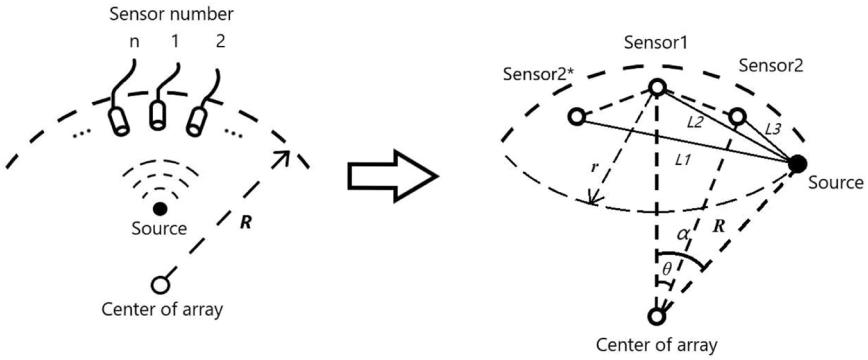

Fig. 5. The geometric relationship between sensors and source.

source, θ is the deflection angle between *Sensor*1 and *Sensor*2, and α is the deflection angle between *Sensor*1 and source. From their geometric relationship, it is easy to see that the distance difference between adjacent sensors reaches its maximum value when the signal source is close to the edge of the sensor array. However, it is not easy to directly determine which one is larger between $(L_1 - L_2)$ and $(L_2 - L_3)$. Therefore, we analyze them based on their geometric relationship. Given θ, R, and r, where θ is typically less than $\frac{\pi}{2}$ and $r \in [2\mathrm{R}\sin\theta, 2\mathrm{R}]$, we can derive the following relationship from geometry:

$$\begin{cases} \alpha = \arcsin\dfrac{r}{2\mathrm{R}} \\ L_3 = 2\mathrm{R}\sin(\alpha - \theta) \\ L_2 = r \\ L_1 = 2\mathrm{R}\sin(\alpha + \theta) \end{cases} \tag{7}$$

Substituting Eq. (7) into the expression $(L_1 - L_2) - (L_2 - L_3)$, we can simplify it to obtain:

$$\begin{aligned} (L_1 - L_2) - (L_2 - L_3) &= 2\mathrm{R}\sin(\alpha + \theta) + 2\mathrm{R}\sin(\alpha - \theta) - 2r \\ &= 4\mathrm{R}\sin\alpha\cos\theta - 2r = 2r(\cos\theta - 1) < 0 \end{aligned} \tag{8}$$

Let V be the sound velocity, ΔT be the time difference between two adjacent sensors receiving the signal, and Δt be the sampling time interval of the sensors. From Eq. (8), $(L_1 - L_2) < (L_2 - L_3)$ can be inferred, and the positional difference Δd of signals originating from the same source in the sampling direction of the matrix space can be obtained:

$$\Delta d = \frac{\Delta T}{\Delta \mathrm{t}} = \frac{L_2 - L_3}{\mathrm{V}\Delta \mathrm{t}} = \frac{r - 2\mathrm{R}\sin\left(\arcsin\frac{r}{2\mathrm{R}} - \theta\right)}{\mathrm{V}\Delta \mathrm{t}} \tag{9}$$

According to the principle of the EGI algorithm, when $d \geq \frac{\Delta d}{2}$, the capture of all fragmented signals can be completed. Considering that in practical applications, the signal source is not located right next to the sensor, and a larger value of d may introduce additional errors,d is taken as $d = \left[\frac{\mathrm{C}\Delta d}{2}\right]$. Here, C is a positive number less than 1, which is used to constrain the search half-width d. The expression for the search half-width d is defined as:

$$d = \left[\mathrm{C}\frac{r - 2\mathrm{R}\sin\left(\arcsin\frac{r}{2\mathrm{R}} - \theta\right)}{2\mathrm{V}\Delta \mathrm{t}}\right] \tag{10}$$

3. Simulation and analysis

3.1. Signal simulation

The PA signals were simulated using the k-wave toolbox based on MATLAB [27]. To better simulate real-world scenarios, we designed a head model with complex structures and grayscale variations, as shown in Fig. 6(a). The original sound pressure distribution generated by the models is shown in Fig. 6(b). The sensor data visualization is shown in Fig. 6(c).

The original sound pressure distribution area was a square of size 120mm × 120mm, and a ring array with a radius of 55mm was used. The ring array was centered at the symmetrical center of the sound pressure distribution area. The simulation grid size was set to 640 × 640, where the size of the medium region was 600 × 600, and the corresponding size of each pixel is 0.2mm × 0.2mm. A perfect matched layer was located at the edge of the sound pressure distribution area with a width of 20. The sound speed of the medium was set to 1500m/s, and the sampling interval was 40ns. In more mature photoacoustic imaging applications, the number of sensors in a ring array is often 256, or 512 [28,29]. High-quality photoacoustic reconstruction images can be obtained with sufficient quality using data at this number. Therefore, in the subsequent

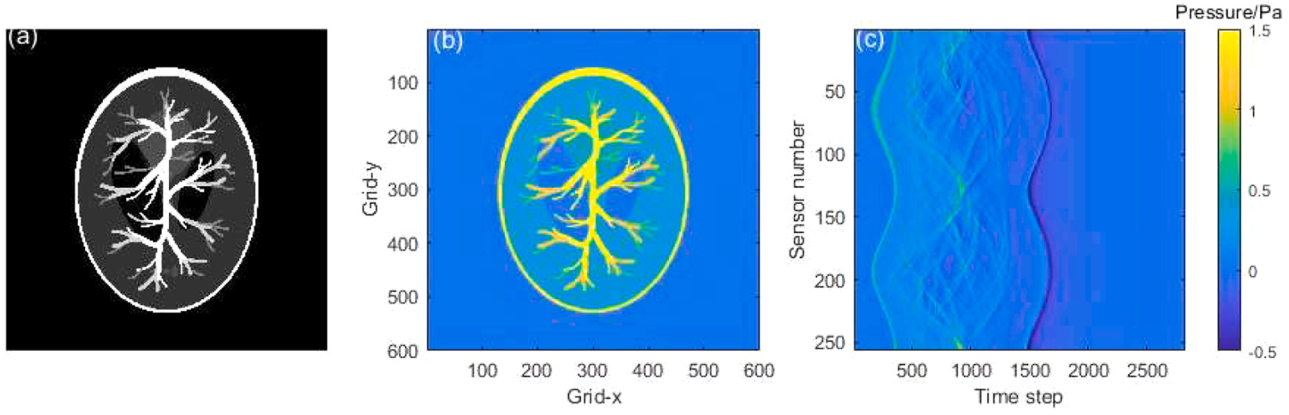

Fig. 6. PA simulation with 256 sensors. (a) Head model; (b) Sound pressure distribution; (c) Sensor data.

simulations and experiments, apart from directly conducting reconstructions (where the number of sensors used for reconstruction is the same as the number of sensors used for forward simulation), the number of sensors used for reconstruction is set to 256 (i.e., the sparse sampled data is processed through an algorithm to make it equivalent to 256 samples).

3.2. EGI processing and reconstruction

Assuming there are m sensors and n total time-domain sampling points, the signal data format is a matrix of size $m \times n$. For the elements in this matrix, the search half-width d is only related to the column number where the element is located. Therefore, in practical calculations, it is only necessary to generate a vector of length n that stores the half-width d according to the order of matrix columns. When performing EGI, the vector can be called directly. This can greatly improve the speed of the interpolation algorithm without the need to recalculate the size of d for each element.

For the simulated signal obtained in Section 3.1, the total number of spatial sampling points is 256. Here, it is reduced to 128 sensors shown in Fig. 7(a). With C = 0.2, we compute d using Eq. (10) and obtain the corresponding search half-width vector shown in Fig. 7(b).

And the reconstruction is carried out using several typical reconstruction algorithms such as BP, DAS, and TR, and the results are shown in Fig. 8.

From the reconstruction results in Fig. 8, it can be seen that the EGI algorithm can significantly suppress image artifacts and improve the quality of photoacoustic reconstruction. Several typical photoacoustic reconstruction algorithms were used in the above simulation, among which the BP algorithm is simple and easy to implement, and has an advantage in imaging larger objects, but the imaging effect is poor for smaller structures or high-frequency components. The DAS algorithm can effectively suppress noise and interference, and has good imaging quality, but requires accurate parameter adjustment and calculation. TR can handle more complex imaging problems, and has good imaging effect on high-frequency components, but has a large calculation amount and is difficult to use in real-time systems. According to the analysis results in reference [25], the interpolation algorithm can provide sufficiently dense signal data to significantly improve the quality of reconstruction results, although its performance may vary among different reconstruction algorithms, the quality of the reconstructed image is still directly related to the data used for reconstruction. Although the choice of reconstruction algorithm has a significant impact on the quality of the imaging, in order to objectively compare the effects of various signal processing algorithms on the reconstruction results, in the algorithm research in the later part of the text, we will use the TR algorithm, which has advantages in imaging details and does not require consideration of data filtering issues, as the basic reconstruction algorithm.

3.3. Effects of noise to EGI

Using a perfect signal without noise does not prove the effectiveness of the algorithm, as various complex factors such as optical absorption, non-uniformity of the light beam, electronic noise, and background noise can affect the signal in practical applications, leading to various forms of noise in the photoacoustic signal [30–32]. To study the performance of the EGI algorithm under the influence of these noise factors, 128 sensors data is used as an example, and two simulation scenarios are mainly considered: point-like random noise and non-uniformity of the signal at the sensor level.

For point-like random noise, additive Gaussian white noise is simulated. The standard deviation is set to 0.2, and the mean is set to 0, with noise proportions of 30 %, 50 %, 70 %, and 90 %, respectively. Then, the EGI algorithm is used for interpolation and the TR algorithm is used for reconstruction, and the results are shown in Figs. 9–10.

Similarly, for the non-uniform noise, the vector along the axis of the data time sampling point is taken as the unit. Multiplying it with a random Gaussian distribution with a mean of 1 and a standard deviation of 0.2, the noise proportions are set to 30 %, 50 %, 70 %, and 90 %, respectively. The EGI algorithm is used for interpolation, and the TR algorithm is used for reconstruction. The results are shown in Figs. 11–12.

From Figs. 9–12, it can be seen that under the influence of both pointwise and non-uniform noise, the EGI algorithm can accurately capture the discontinuities in the signal and insert signal values at appropriate locations. Even in the case where the noise proportion is as high as 90 %, the algorithm can effectively restore the details of the image and suppress the generation of artifacts.

The results show that the EGI algorithm is not sensitive to noise. Although the EGI algorithm cannot directly remove the inherent noise in the sampled signal, the noise is smoothed to some extent from the results. In practical applications, various methods can be used to reduce noise and calibrate sensor amplitudes, and combined with the EGI algorithm, can achieve relatively ideal interpolation results.

3.4. Comparison of sparse reconstruction

In practical applications, interpolation methods are commonly used

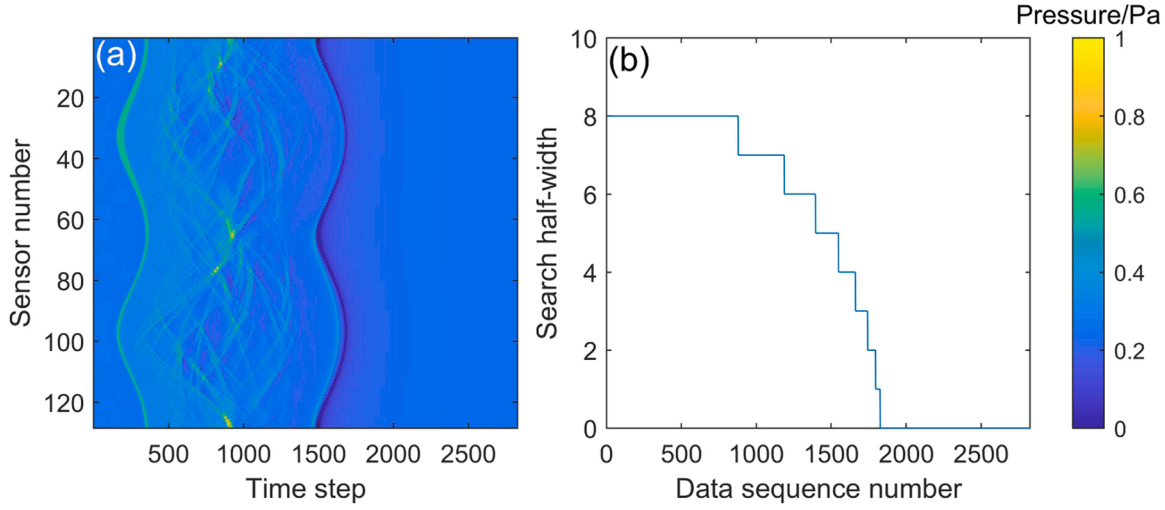

Fig. 7. Signal processed with EGI. (a) Data with 128 sensors; (b) Vector of search half-width.

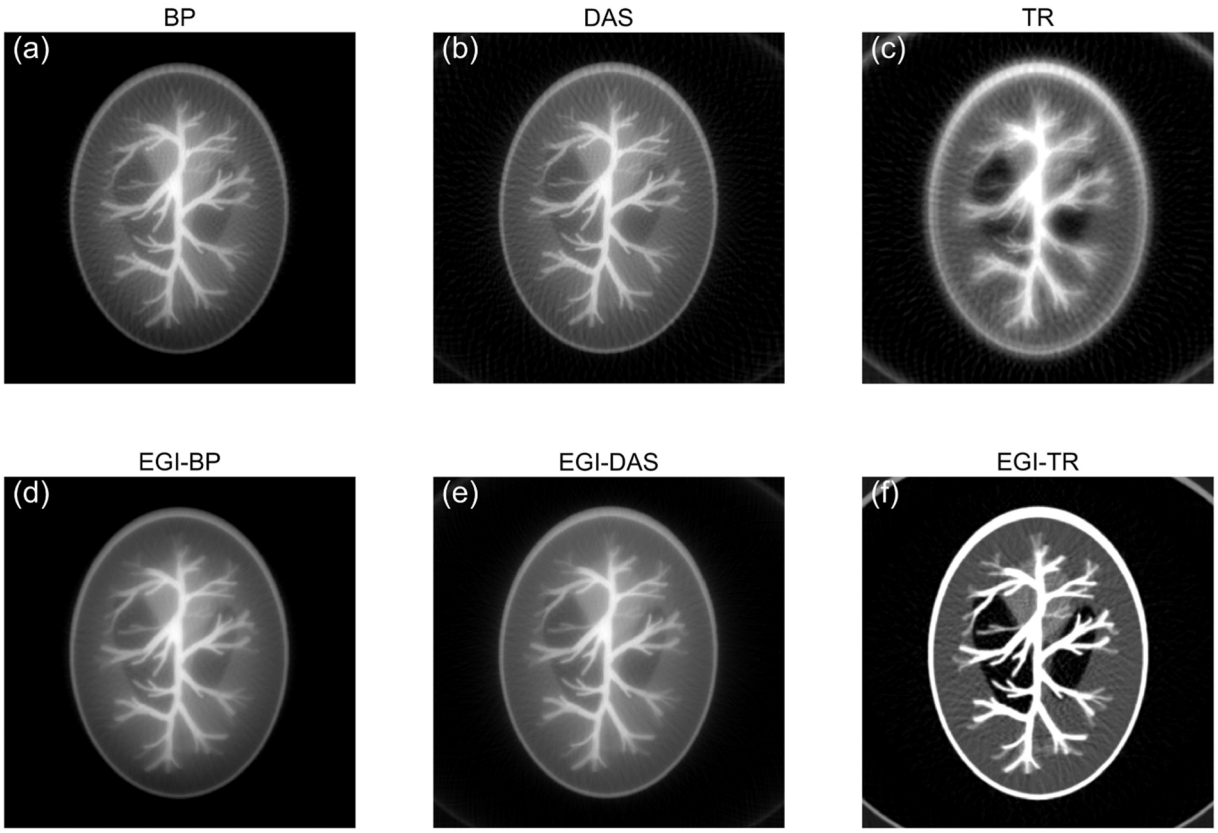

Fig. 8. PA reconstruction with 128 sensors. (a) Reconstruction with BP; (b) Reconstruction with DAS; (c) Reconstruction with TR; (d) Reconstruction with EGI and BP; (e) Reconstruction with EGI and DAS; (f) Reconstruction with EGI and TR.

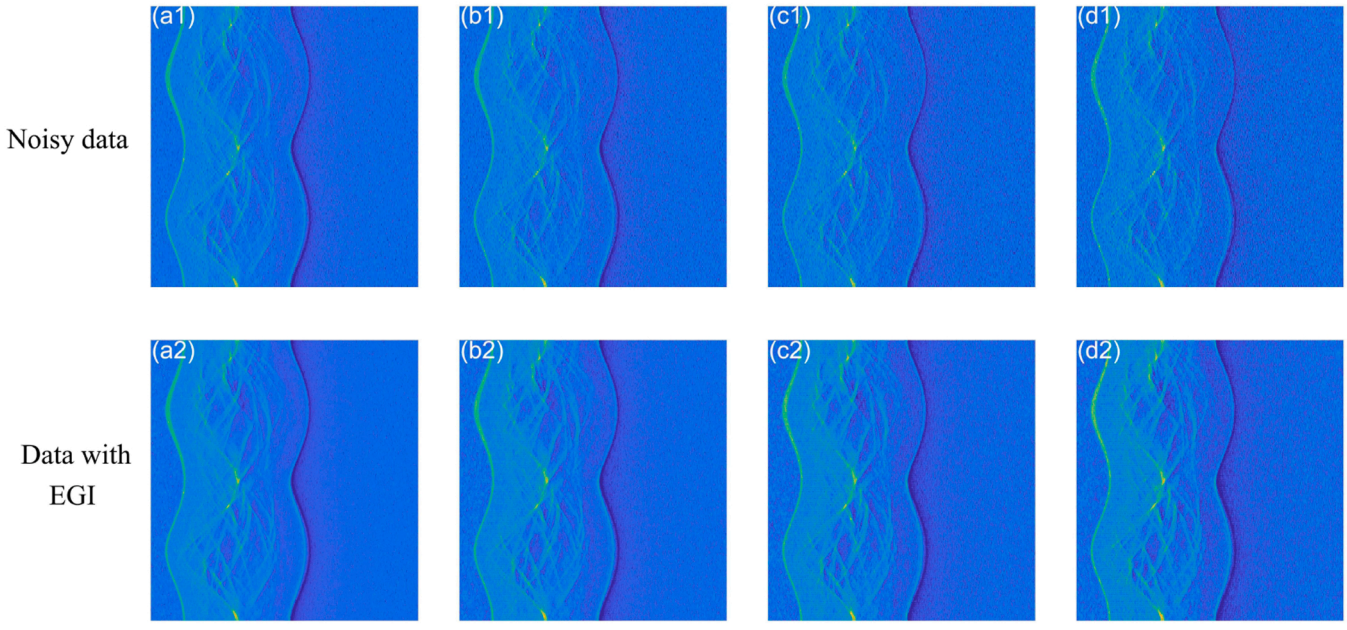

Fig. 9. Interpolation of data with random noise at 128 sensors. (a1–a2) Noise proportions of 30 %; (b1–b2) Noise proportions of 50 %; (c1–c2) Noise proportions of 70 %; (d1–d2) Noise proportions of 90 %.

to process sparsely sampled data to improve the performance of PA reconstruction. In [25], the researchers explained the cause of reconstruction artifacts and demonstrated that interpolation methods can generate a sufficiently dense grid for numerical computations, thus reducing reconstruction artifacts.

According to the conclusion in [17], traditional interpolation methods such as NI, LI, and SI have similar performance in PA reconstruction and produce comparable improvements in reconstructed images. Therefore, only the NI method was selected for comparison among traditional methods. When using the NEDI method to process images, it

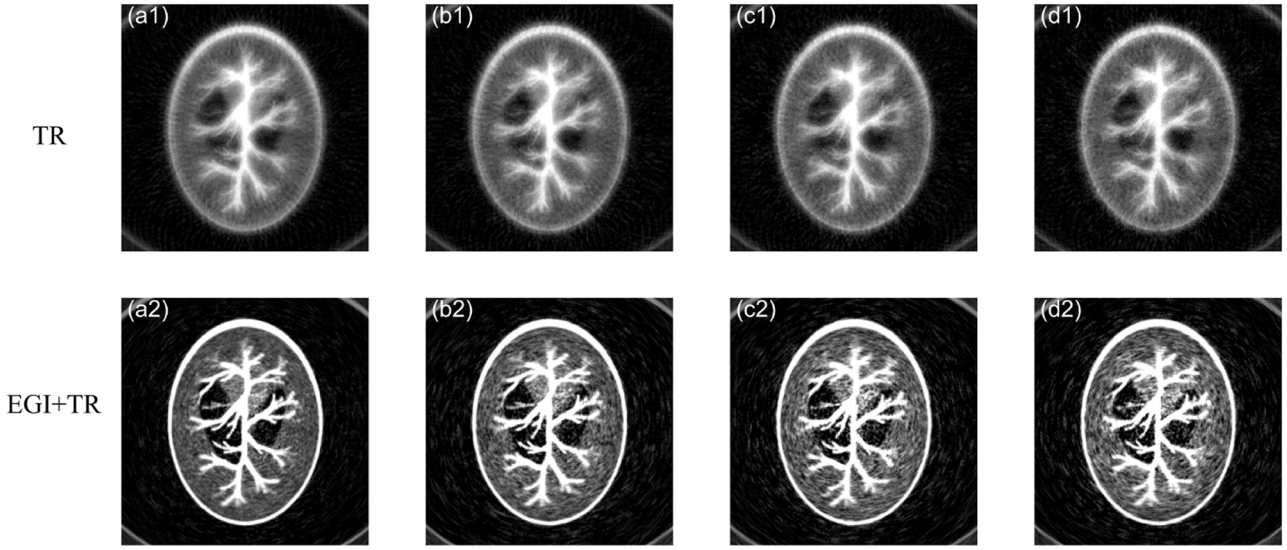

Fig. 10. Reconstruction of data with random noise at 128 sensors. (a1–a2) Noise proportions of 30 %; (b1–b2) Noise proportions of 50 %; (c1–c2) Noise proportions of 70 %; (d1–d2) Noise proportions of 90 %.

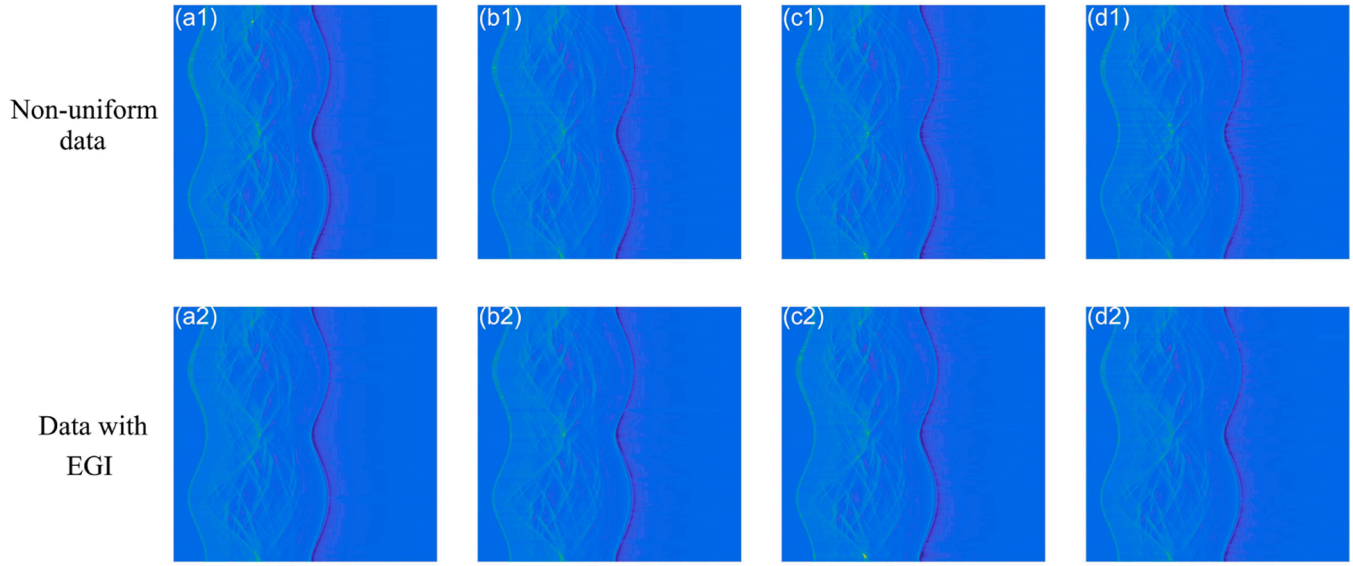

Fig. 11. Interpolation of data with non-uniformity at 128 sensors. (a1–a2) Noise proportions of 30 %; (b1–b2) Noise proportions of 50 %; (c1–c2) Noise proportions of 70 %; (d1–d2) Noise proportions of 90 %.

usually produces more effective interpolation results than traditional algorithms in images with rich edge information. Following the method in Ref. [20], a window size of 8 × 8 is chosen, and a local variance threshold set to 8. When using CS algorithm to recover sparse signals, since the photoacoustic signal is sparse in spatial domain, the two-dimensional photoacoustic signal is unfolded into one dimension along the spatial sampling direction., following the approach described in references [21,22], the signal recovery problem is formulated as a constrained optimization problem with l_1 norm regularization. The recovery of the signal is formulated as the solution to the underdetermined equation, and the CVX toolbox [33] is used for the computation. Due to the characteristics of the circular array photoacoustic data, random selection of matrix data row vectors (a unit row vector is the complete temporal sampling data of a sensor) is used here for random sampling. Therefore, the observation matrix is constructed based on the corresponding sampling method. And the discrete cosine transform matrix is chosen to be the sparse matrix.

The number of sensors was reduced to 96, 80, 64, 48 and 32. The noise was set according to the settings in Section 3.3, with both noise levels set to 30 %, and other parameters unchanged. NI, NEDI, CS, and EGI algorithms were used to process the signal. The signal processing results are shown in Fig. 13, and the reconstruction results obtained using the TR algorithm are shown in Fig. 14.

To objectively evaluate the performance of each algorithm, the image quality score was calculated using the original sound pressure distribution shown in Fig. 6(b) as a reference. And the results were obtained with image quality assessment (IQA) algorithm, including PSNR, SSIM, and MSE [34,35], as shown in Table 1 and Fig. 15.

From the results in Figs. 14–15, it can be seen that when using the NI algorithm, good imaging quality can be obtained at higher sampling rates, but as the sampling decreases, the image details deteriorate significantly, accompanied by obvious edge blur. When using the NEDI algorithm, good imaging results were also obtained at higher sampling rates, with fewer artifacts compared to the NI algorithm results, but

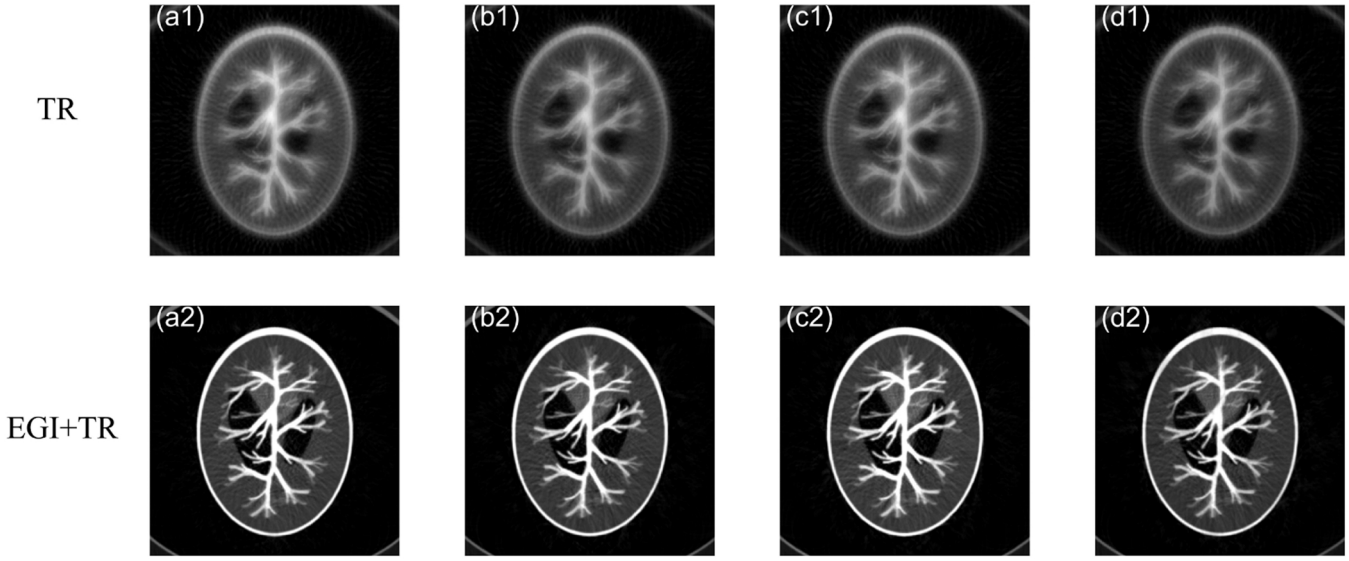

Fig. 12. Reconstruction of data with non-uniformity at 128 sensors. (a1–a2) Noise proportions of 30 %; (b1–b2) Noise proportions of 50 %; (c1–c2) Noise proportions of 70 %; (d1–d2) Noise proportions of 90 %.

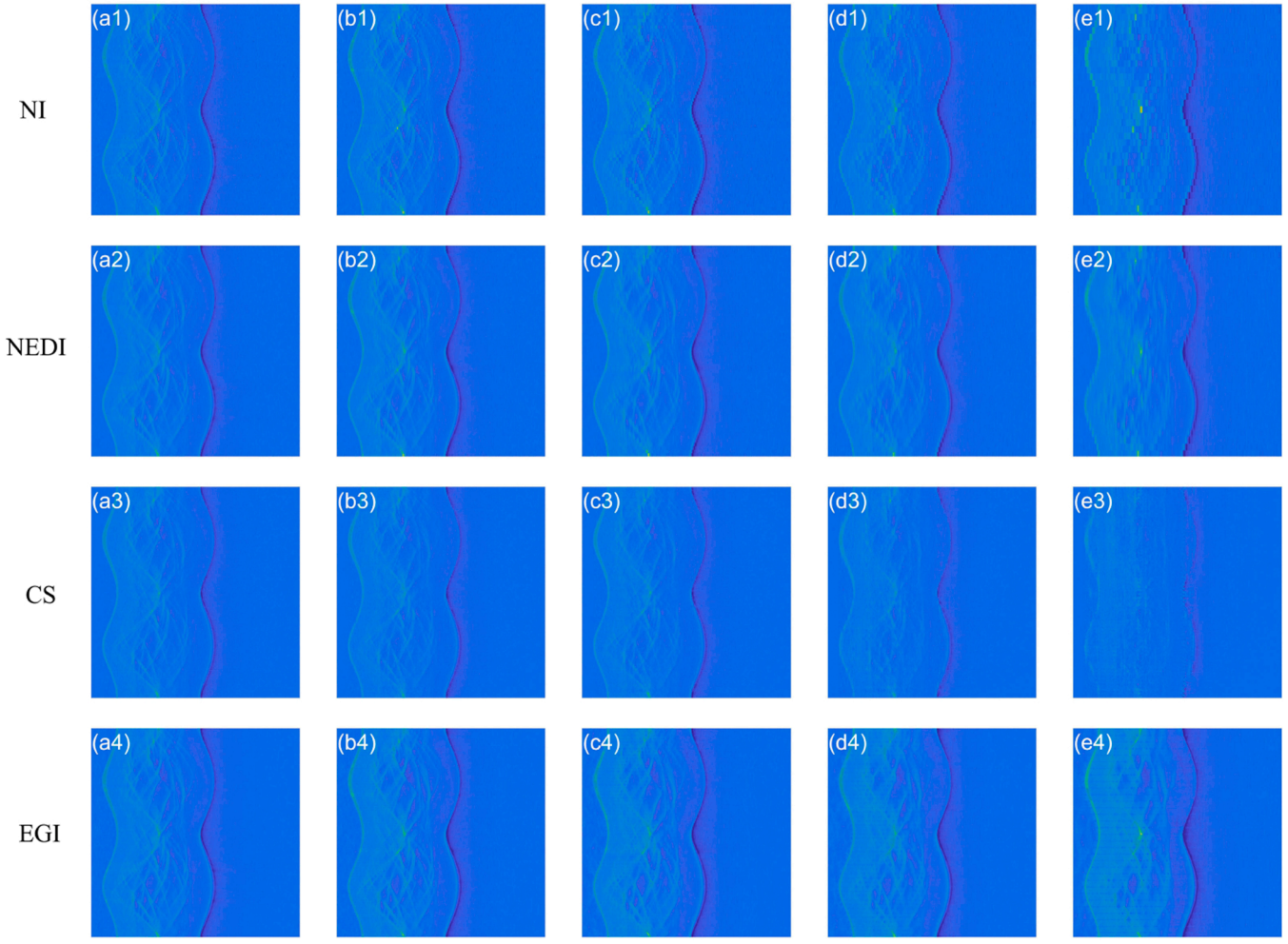

Fig. 13. Signal processing results under different sparsity levels. (a1–a4) 96 sensors; (b1–b4) 80 sensors; (c1–c4) 64 sensors; (d1–d4) 48 sensors; (e1–e4) 32 sensors.

more edge details were lost when the sampling was reduced. When the CS algorithm was used to process the data, the imaging details obtained at higher sampling rates were slightly better than NI and NEDI under 96 sensors. However, due to the sensitivity of the algorithm to noise, additional noise appeared in the processed signal, which had an adverse effect on the reconstruction results. As the sparsity level increased, the

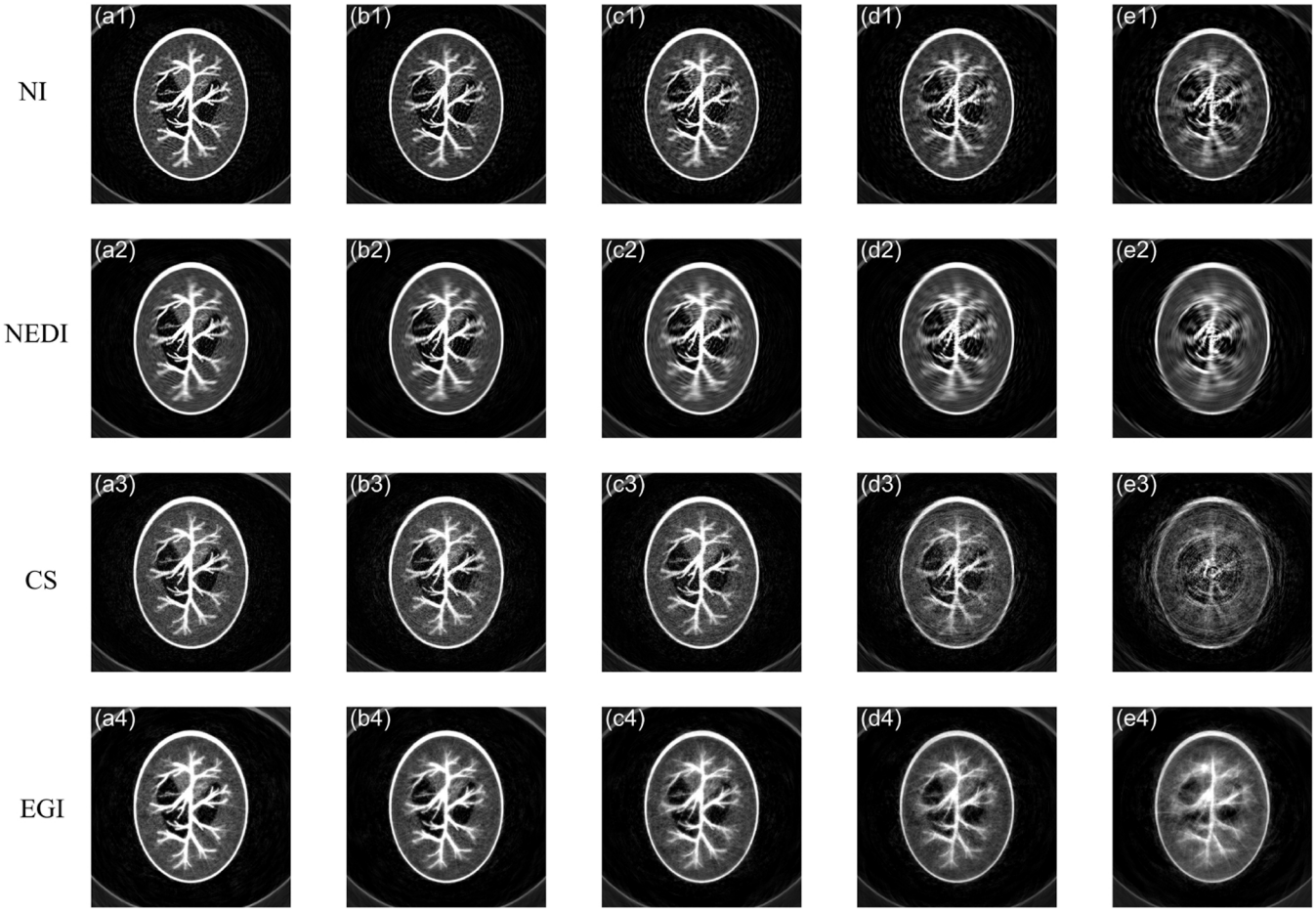

Fig. 14. TR reconstruction results under different sparsity levels. (a1–a4) 96 sensors; (b1–b4) 80 sensors; (c1–c4) 64 sensors; (d1–d4) 48 sensors; (e1–e4) 32 sensors.

Table 1
IQA results of TR reconstructions.

IQA methods	Interpolation methods	Number of sensors				
		96	80	64	48	32
PSNR/dB	NI	19.5167	17.7612	16.2132	15.2602	13.8233
	NEDI	18.9366	17.5055	17.2001	15.4960	13.5643
	CS	18.5475	17.5822	17.0671	14.3969	11.5774
	EGI	21.6137	20.1614	19.0232	17.9311	16.5161
SSIM	NI	0.6216	0.6394	0.6092	0.6077	0.5986
	NEDI	0.7265	0.7243	0.6924	0.6729	0.6566
	CS	0.7238	0.6805	0.5965	0.5408	0.4783
	EGI	0.7295	0.7183	0.7213	0.7083	0.6817
MSE	NI	0.0111	0.021	0.0189	0.0297	0.0414
	NEDI	0.0127	0.0177	0.019	0.0282	0.0440
	CS	0.0139	0.0174	0.0196	0.0363	0.0695
	EGI	0.0068	0.0096	0.0125	0.0161	0.0223

CS algorithm became increasingly difficult to recover the original signal from the observed signal, resulting in a significant drop in the quality of the reconstruction results. Without using a denoising algorithm, the EGI algorithm produced results with less noise than other algorithms, and could still recover image details well as the sparsity level increased. This indicates that the EGI algorithm performs better than other algorithms in sparse sampling photoacoustic reconstruction.

It should be noted that as the sparsity level increases, the image quality of the results obtained by several algorithms decreases to varying degrees. When using the NI, NEDI, and CS algorithms, this deterioration in image quality is mainly manifested as the loss of image details and the increase of image artifacts, but the situation is different for the EGI algorithm. For the EGI algorithm, the deterioration in image quality is mainly manifested as the diffusion of strong signals, which corresponds to the principle of the EGI algorithm. The sparsity of the signal is manifested in the sinogram as the tearing of the signal band. Since the EGI algorithm has captured the vast majority of the torn signal, the errors in the results obtained by this algorithm mainly come from those incorrectly connected signals, and as the sparsity level increases, the errors of this kind also increase. However, Eq. (3) determines that the EGI algorithm tends to choose smaller values, so as the number of iterations increases, strong signal values will be excluded, making the diffusion of strong signals only related to the sparsity level. Therefore, this type of error is convergent, and the IQA results show that the EGI

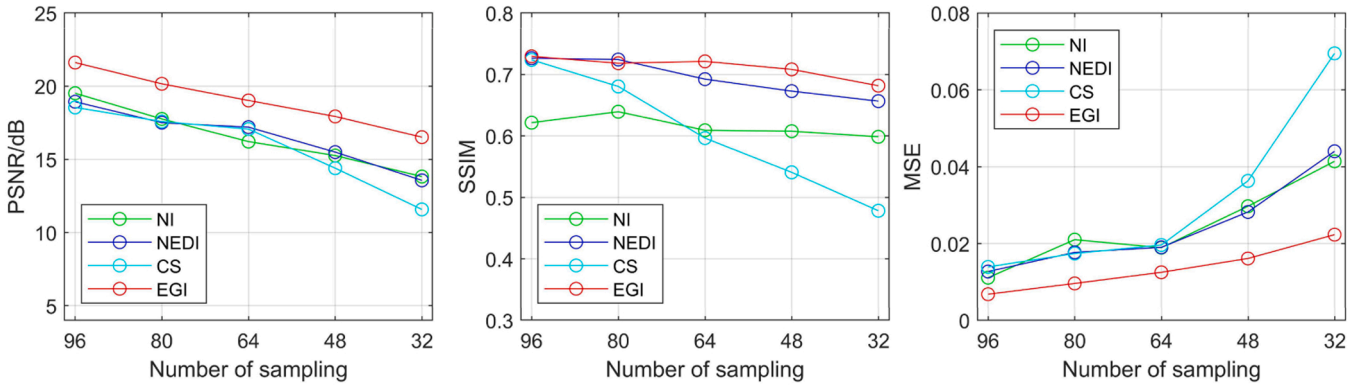

Fig. 15. Comparison of IQA results of NI, NEDI, CS, and EGI.

algorithm performs better at the same sparsity level.

In addition, for photoacoustic imaging, researchers generally use methods such as adjusting the wavelength and using contrast agents to enhance the absorption of the photoacoustic signal by the region of interest. In this scenario, the advantage of the EGI algorithm lies in its ability to prioritize the integrity of structures corresponding to strong signals. This feature can assist researchers in reconstructing target structures using fewer sensors than normal sparse conditions.

3.5. Computational complexity

Assuming there are m sensors and n total time-domain sampling points, generally $n \gg m$. The number of iterations for interpolation using the EGI method is denoted as N. To analyze the time complexity of the EGI algorithm, let $T(k)$ denote the time complexity of the EGI algorithm, $f(k)$ be the problem size function, and k represent the problem size. Then we have $T(k) = O[f(k)]$. According to the EGI algorithm, the first layer of calculations involves taking the smaller value between two symmetric elements and performing two loops. The second layer searches within a half-width of d, and performs $2d+1$ loops. The third layer traverses a vector of length n, although linear interpolation is used for edge processing, it has little effect on the time complexity, and is still approximated as n loops. The fourth layer traverses a total of m rows of vectors. Since m doubles after each iteration, when the number of interpolation iterations is N, a total of $m(2^N - 1)$ loops are performed. Therefore, the problem size function of the EGI algorithm can be represented as $f(m,n,N) = 2(2d+1)nm(2^N - 1)$. If d tends to converge after N iterations, then d can be treated as a constant, and the time complexity can be obtained:

$$T(m,n,N) = O\left(2^N mn\right) \tag{11}$$

It can be seen that when the number of iterations N remains unchanged, the time complexity of the EGI algorithm can be considered linear. However, as the number of iterations increases, its time complexity will increase exponentially.

Next, we compare the processing time of the NI, NEDI, CS and EGI algorithms for data processing. The simulations were performed on a desktop computer with a Windows 10 operating system, an i7-11700 CPU with a clock frequency of 2.5 GHz, and a memory capacity and frequency of 32 GB and 3200 MHz, respectively. Take simulated PA signal data from sensors with quantities of 32, 48, 64, 80, and 96, and interpolate them to be equivalent to 256 sensors. It should be noted that the interpolation factor of the NEDI algorithm is 2^N. The EGI algorithm performs interpolation iteratively, and its interpolation factor is similar to that of the NEDI algorithm, which is also 2^N, where N is a positive integer. When using NEDI and EGI algorithms for processing, the interpolation factor is 4, and the parts that are less than 256 samples are filled using NI. As the data size increases, the computation required by CS algorithms increases drastically. Considering the high sampling frequency of the signal, when using CS algorithms to process the signal, the temporal dimension of the data is compressed by a factor of 0.5 to reduce the computational load. The results are shown in the Table 2 and Fig. 16.

As can be seen from the table, with an increase in the number of iterations, the EGI algorithm's computation time increases, which is consistent with the analysis of time complexity mentioned earlier. However, this algorithm can still process data at a relatively fast speed even under low interpolation rate. Therefore, in practical applications, the EGI algorithm can be used for the initial iterations of data processing, and simple algorithms such as NI can be used for processing when equivalent to higher density sampling. This approach can greatly accelerate the data processing speed while maintaining a high level of interpolation quality.

3.6. Experimental data reconstruction

In the experiment, a circular array is used for photoacoustic imaging of a phantom composed of agar blocks and leaf veins. The experimental setup, phantom, and schematic diagram are shown in Fig. 17.

The circular transducer array has a radius of 50 mm and a sampling frequency of 40 MHz. The excitation source uses an optical parametric oscillator (SOLAR LP604), the wavelength of the excitation light is set to 680 nm, and the maximum energy density on the surface is about 4mJ/cm^2. The light beam is expanded and coupled to a fiber optic bundle, forming an annular illumination field at the focal plane of the transducer array. The system is controlled by a high-precision delay generator (Stanford Research Systems, DG645).

Due to the huge amount of computation and time is required for precise reconstruction using the TR algorithm. For efficiency considerations, the DAS algorithm was used to reconstruct the photoacoustic image. The accuracy of the reconstructed image was 0.05 mm, and the size of the reconstructed image was 2000 × 2000. The size of the target area was set to 800 × 800, and its center coincided with the center of the reconstructed image. The original signal was sampled with 128 sensors and processed using NI, NEDI, CS, and EGI to make it equivalent to 256 sampling, and then reconstructed using DAS algorithm. The results of data processing and image reconstruction are shown in Figs. 18–19.

Based on the signal processing results of the experimental data in

Table 2
Time cost.

Data size	NI (s)	NEDI (s)	CS (min)	EGI (s)
32 × 2829	0.0533	14.5005	~ 3	1.9301
48 × 2829	0.0539	25.3241	~ 5	2.0119
64 × 2829	0.0553	32.9577	~ 6	2.0706
80 × 2829	0.0561	47.0933	~ 8	2.1748
96 × 2829	0.0578	55.9613	~ 11	2.2098

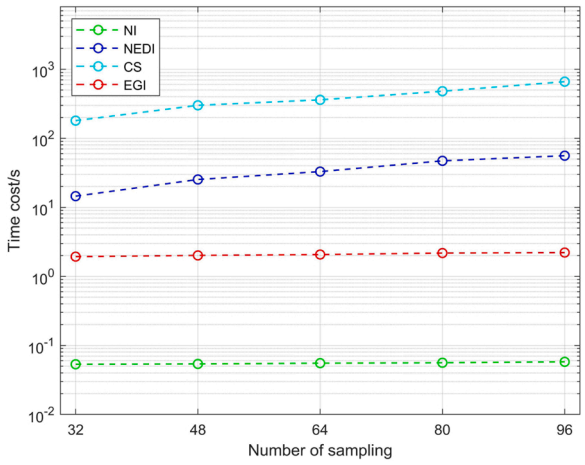

Fig. 16. Comparison of time cost of NI, NEDI, CS, and EGI.

Fig. 18, the performance of the NI and NEDI algorithms is consistent with the simulation results. However, due to the strong noise in the experimental signal, the performance of the CS algorithm is slightly worse than the simulation, making it difficult to recover the complete original signal from the sparse signal. Based on the reconstruction results in Fig. 19, the main problems with the NI and NEDI algorithms are the blurring of the image edges and image artifacts, while the CS algorithm performs better at the image edges than the NI and NEDI algorithms, but the additional noise in the reconstructed signal leads to the loss of some image details. The EGI algorithm performs better than other algorithms in the reconstructed image, as it not only ensures the integrity of the structural details of the image, but also better suppresses the generation of image artifacts and noise.

4. Conclusion

Sparse sampling in photoacoustic imaging is one of the main factors affecting the quality of reconstructed images. In this paper, we analyze the geometric physical relationship between adjacent sensor signals based on a circular array, establish the mathematical relationship between the deviation of the signal matrix in the time domain direction and the number of time sampling points, and propose an extremum-guided interpolation (EGI) algorithm. By utilizing the simple prior information of the continuity of the photoacoustic signal, the EGI algorithm can estimate high sampling rate signals without complex constrained solving or operator calculations, only through nonlinear approximation. Simulation and experimental data validation show that the EGI algorithm is not sensitive to noise, can effectively improve the quality of actual photoacoustic reconstruction, and has a relatively fast computation speed, which is advantageous for its application in real-time systems. We hope to further improve the proposed algorithm in future work to increase its speed and performance.

CRediT authorship contribution statement

Haoyu Wang: Conceptualization, Methodology, Software, Investigation, Formal Analysis, Writing – Original Draft. **Yan Luo:** Experimental Execution, Data Collection. **Cheng Ma:** Experiment Design, Resource Integration, Experimental Guidance & Oversight. **Yiping Han:**

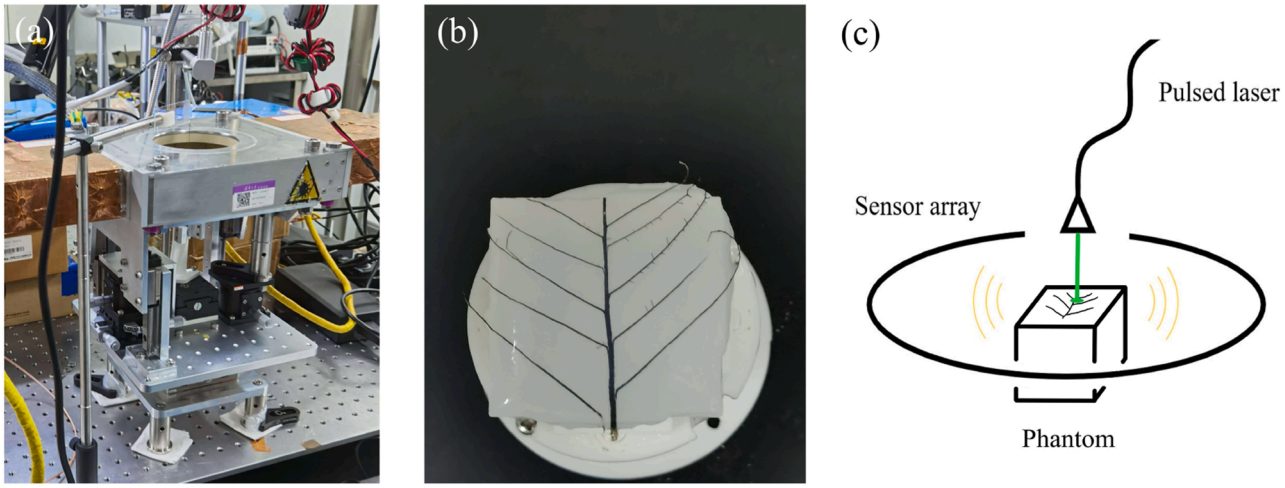

Fig. 17. The experimental setup and schematic diagram. (a) Experimental setup; (b) Phantom; (c) Schematic diagram.

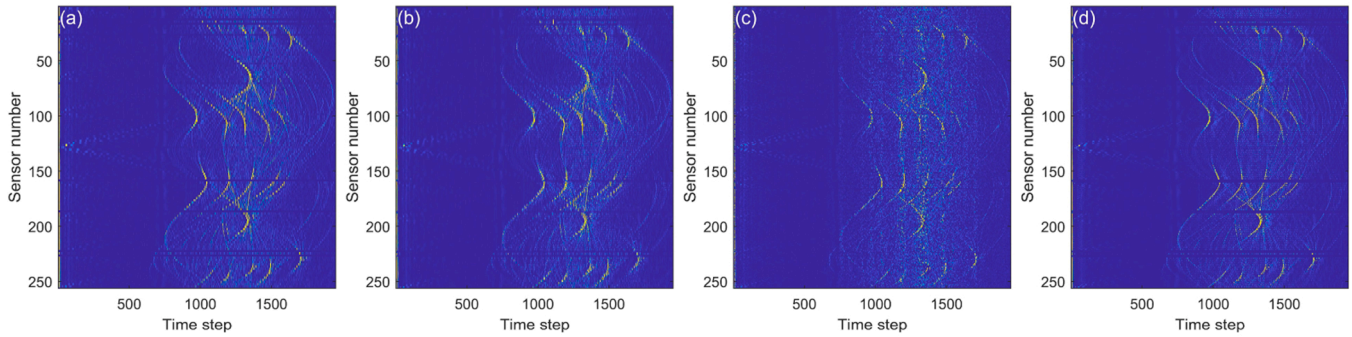

Fig. 18. Signal processing results of experimental data. (a) NI; (b) NEDI; (c) CS; (d) EGI.

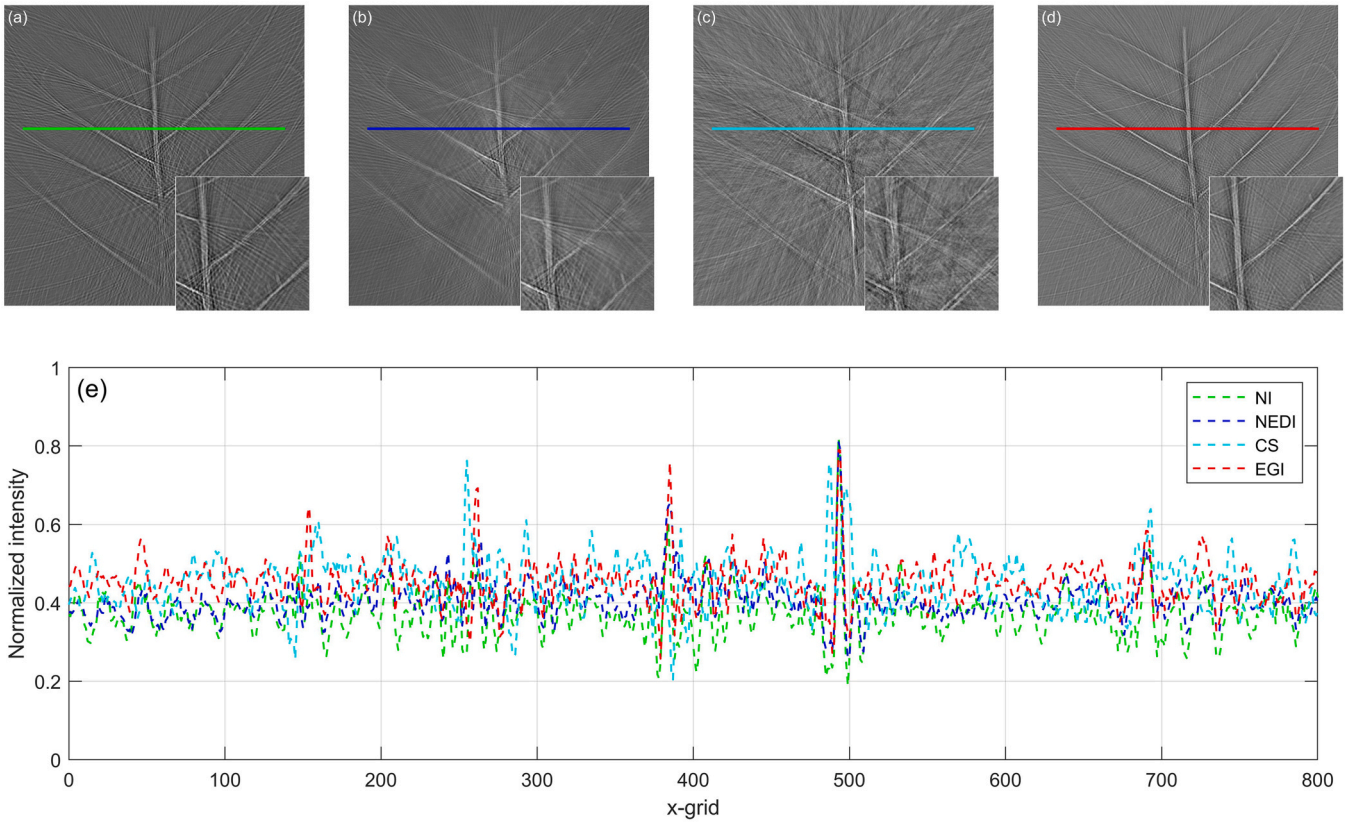

Fig. 19. Reconstruction results with DAS of experimental data. (a) Reconstruction with NI; (b) Reconstruction with NEDI; (c) Reconstruction with CS; (d) Reconstruction with EGI; (e)Comparison of image rows.

Resources, Supervision, Writing – Review & Editing.

Funding

This work was supported by National Key Laboratory Foundation of China (Y19-SYSJJ-61424110301).

Declaration of Competing Interest

The authors declared no potential conflicts of interest with respect to the research, authorship, and publication of this article.

Data Availability

Data will be made available on request.

References

[1] Alexander Graham Bell, On the production and reproduction of sound by light, Am. J. Sci. 3 (118) (1880) 305–324.
[2] Sergey A. Telenkov, Andreas Mandelis, Photothermoacoustic imaging of biological tissues: maximum depth characterization comparison of time and frequency-domain measurements, J. Biomed. Opt. 14 (4) (2009) (044025-044025).
[3] Lihong V. Wang, Prospects of photoacoustic tomography, Med. Phys. 35 (12) (2008) 5758–5767.
[4] Minghua Xu, Lihong V. Wang, Photoacoustic imaging in biomedicine, Rev. Sci. Instrum. 77 (4) (2006), 041101.
[5] Frank Dennerlein, et al., Fan-beam filtered-backprojection reconstruction without backprojection weight, Phys. Med. Biol. 52 (11) (2007) 3227.
[6] Mathias Fink, Claire Prada, Acoustic time-reversal mirrors, Inverse Probl. 17 (1) (2001) R1.
[7] Yulia Hristova, Peter Kuchment, Linh Nguyen, Reconstruction and time reversal in thermoacoustic tomography in acoustically homogeneous and inhomogeneous media, Inverse Probl. 24 (5) (2008), 055006.
[8] Yuan Xu, Lihong V. Wang, Time reversal and its application to tomography with diffracting sources, Phys. Rev. Lett. 92 (3) (2004), 033902.
[9] Ebrahim Najafzadeh, et al., Photoacoustic image improvement based on a combination of sparse coding and filtering, J. Biomed. Opt. 25 (10) (2020), 106001.
[10] Katheryne E. Wilson, Tzu Yin Wang, Jürgen K. Willmann, Acoustic and photoacoustic molecular imaging of cancer, J. Nucl. Med. 54 (11) (2013) 1851–1854.
[11] Parastoo Farnia, et al., Dictionary learning technique enhances signal in LED-based photoacoustic imaging, Biomed. Opt. Express 11 (5) (2020) 2533–2547.
[12] Tri Vu, et al., Deep image prior for undersampling high-speed photoacoustic microscopy, Photoacoustics 22 (2021), 100266.
[13] Scott H. Holan, John A. Viator, Automated wavelet denoising of photoacoustic signals for circulating melanoma cell detection and burn image reconstruction, Phys. Med. Biol. 53 (12) (2008) N227.
[14] Yi Wang, et al., Photoacoustic imaging with deconvolution algorithm, Phys. Med. Biol. 49 (14) (2004) 3117.
[15] Lu Tao, Li Xiujuan, Wang Huiyou, Photoacoustic tomography with Wiener filter deconvolution algorithm, Acta Opt. Sin. 29 (7) (2009) 1854–1857.
[16] Sun Zheng, Han Duoduo, Yuan Yuan, 2-D image reconstruction of photoacoustic endoscopic imaging based on time-reversal, Comput. Biol. Med. 76 (2016) 60–68.
[17] Avijit Paul, et al., Exploring polynomial based interpolation schemes for photoacoustic tomographic image reconstruction, Biomed. Phys. Eng. Express 8 (1) (2021), 015019.
[18] Jens Horstmann, et al., Full-field speckle interferometry for non-contact photoacoustic tomography, Phys. Med. Biol. 60 (10) (2015) 4045.
[19] Xin Li, Michael T. Orchard, New edge-directed interpolation, IEEE Trans. Image Process. 10 (10) (2001) 1521–1527.
[20] Yong Liu, Research on the effect of new edge-directed interpolation on CT image quality, J. Sci. Teach.'s Coll. Univ. 41 (8) (2021) 8–14 (in Chinese).
[21] Simon Arridge, et al., Accelerated high-resolution photoacoustic tomography via compressed sensing, Phys. Med. Biol. 61 (24) (2016) 8908.
[22] Xueting Zhang, et al., Sparse-sampling photoacoustic computed tomography: deep learning vs. compressed sensing, Biomed. Signal Process. Control 71 (2022), 103233.
[23] Mingjian Sun, et al., Time reversal reconstruction algorithm based on PSO optimized SVM interpolation for photoacoustic imaging, Math. Probl. Eng. 2015 (2015).
[24] Navchetan Awasthi, et al., Sinogram super-resolution and denoising convolutional neural network (SRCN) for limited data photoacoustic tomography, arXiv Prepr. arXiv 2001 (06434) (2020).
[25] Peng Hu, et al., Spatiotemporal antialiasing in photoacoustic computed tomography, IEEE Trans. Med. Imaging 39 (11) (2020) 3535–3547.

[26] Jonathan M. Cannata, et al., Design of efficient, broadband single-element (20–80 MHz) ultrasonic transducers for medical imaging applications, IEEE Trans. Ultrason. Ferroelectr. Freq. Control 50 (11) (2003) 1548–1557.
[27] Bradley E. Treeby, Benjamin T. Cox, k-Wave: MATLAB toolbox for the simulation and reconstruction of photoacoustic wave fields, J. Biomed. Opt. 15 (2) (2010), 021314.
[28] Jun Xia, et al., Whole-body ring-shaped confocal photoacoustic computed tomography of small animals in vivo, J. Biomed. Opt. 17 (5) (2012), 050506-050506.
[29] Yachao Zhang, Lidai Wang, Video-rate full-ring ultrasound and photoacoustic computed tomography with real-time sound speed optimization, Biomed. Opt. Express 13 (8) (2022) 4398–4413.
[30] Gokhan Guney, et al., Comparison of noise reduction methods in photoacoustic microscopy, Comput. Biol. Med. 109 (2019) 333–341.
[31] Scott H. Holan, John A. Viator, Automated wavelet denoising of photoacoustic signals for circulating melanoma cell detection and burn image reconstruction, Phys. Med. Biol. 53 (12) (2008) N227.
[32] Rayyan Manwar, Mohsin Zafar, Qiuyun Xu, Signal and image processing in biomedical photoacoustic imaging: a review, Optics 2 (1) (2020) 1–24.
[33] M. Grant, S. Boyd, Y. Ye, CVX Users' Guide, 2009. online: ⟨http://www.stanford.edu/boyd/software.html⟩.
[34] Alain Hore, Djemel Ziou, Image quality metrics: PSNR vs. SSIM, in: Proceedings of the 2010 20th International Conference on Pattern Recognition, IEEE, 2010.
[35] Umme Sara, Morium Akter, Mohammad Shorif Uddin, Image quality assessment through FSIM, SSIM, MSE and PSNR—a comparative study, J. Comput. Commun. 7 (3) (2019) 8–18.

Haoyu Wang received the B.S. degree in Electronic Information Science from Xidian University, Shaanxi, China, in 2021 and is currently pursuing a master's degree in Electronic Information at Xidian University, Shaanxi, China. His research interests include image processing, photoacoustic imaging.

Yan Luo received the B.S. degree in Electronic Engineering from Tsinghua University, Beijing, China, in 2020 and is currently pursuing a master's degree in Electronic Engineering at Tsinghua University, Beijing, China. Her major research interest is in photoacoustic tomography.

Yiping Han, Doctoral supervisor, received the B.S. degree in Laser Physics from Northwest University in 1984, a master's degree in Electronic Physics and Devices from Xidian University in 1989, and a Ph.D. in Electromagnetic Field and Microwave Technology from Xidian University in 2000. From 2001 to 2002, she worked on teaching and research related to the propagation and scattering of electromagnetic waves and light waves in media, laser particle size analysis, and applications at the French National Center for Scientific Research.

Cheng Ma received his B.S. degree in Electronic Engineering from Tsinghua University and his Ph.D. degree in Electrical and Computer Engineering from Virginia Tech. Currently, he holds the position of an associate professor at the Department of Electronic Engineering, Tsinghua University. His research interests lie in the field of biomedical optics, especially photoacoustic imaging. Dr. Ma's lab focuses on developing photoacoustic tomography systems, their underlying hardware, algorithms, as well as exploring clinical and biological applications of this new imaging modality.